

Adaptive Integrated Particle Filter for Lightweight Matching Localization Based on Magnetic Map and Inertial Sensors

Gongxu Liu^{ID}, Member, IEEE, Haojie Fan, Yang Ji, Lu Huang^{ID}, Member, IEEE,
and Long Li^{ID}, Senior Member, IEEE

Abstract—Magnetic map matching localization has various strategic applications, such as drone reconnaissance, submarine navigation, cruise missile guidance, etc. However, the complexity of matching localization architectures based on magnetic map often fails to meet the fast position update frequency demands for high-speed moving targets. To address this issue, this article proposes a lightweight matching localization architecture, i.e., an adaptive integrated particle filter (AIPF) method based on magnetic map and inertial sensors. The AIPF method includes the prediction phase, correction phase, normalization phase, integration phase, and estimation phase. By pre-establishing a Bayesian probability integral table (BPIT) based on standard normal probability distribution functions and expectation functions, the integration results can be directly queried from the BPIT adaptively, avoiding the time consuming integration operation when matching the potential magnetic fingerprint. The heading and step length can be obtained by dead reckoning based on inertial sensors. Extensive experiments show that when the heading uncertainty is less than 1.2°, or the step length uncertainty is less than 30% of the precision of reference magnetic map, the AIPF method has comparable positioning accuracy while the computational complexity is reduced to one-tenth of that in the compared methods, such as particle filter, the adaptive optimization firefly algorithm, extended Kalman particle filter, etc. Moreover, when the experimental condition is more challenging, the AIPF method demonstrates better robustness than the compared methods. This work provides a new solution for lightweight matching localization algorithms using magnetic maps and inertial sensors, suitable for various applications requiring high position update frequencies or fast target localization and tracking.

Index Terms—Dead reckoning, Gaussian process regression (GPR), inertial sensors, magnetic map, matching positioning, particle filter.

I. INTRODUCTION

IN GLOBAL navigation satellite system (GNSS) denied conditions, matching localization based on magnetic maps is considered a potential important approach without long-term cumulative errors [1], [2], [3], [4].

As shown in Fig. 1, the magnetic map is composed of magnetic nodes that are topologically arranged in space, and each magnetic node represents magnetic fingerprint, which includes position stamp (such as longitude, latitude, and height) associated with magnetic features, such as magnetic field modulus, horizontal intensity, vertical strength, eastward component, northward component, magnetic heading angle, magnetic inclination, magnetic declination, others, etc [5], [6], [7]. In principle, each magnetic fingerprint needs to satisfy three basic conditions, i.e., measurability, stability and uniqueness. The above are the default conditions for offline magnetic map construction [5], [8] and online magnetic map-based matching localization [9], [10].

The fact that magnetic fingerprints are unique is an over-idealized requirement, since magnetic distortions do not exist everywhere in the physical environment, making magnetic fingerprints globally ambiguous in magnetic maps. Therefore, magnetic sensors are often used for joint localization with other sensors (such as inertial sensors, vision sensors, etc.) in matching localization. The proximity-point-features matching localization method is proposed in the geomagnetic matching [11]. Wang et al. [12] proposed the extended Kalman filter (EKF) for matching positioning based on magnetic maps and inertial sensors. The matching localization methods based on the fusion of particle filtering (PF) and pedestrian dead reckoning (PDR) are the most common, however the uncertainty in direction or step length estimation can introduce extra location errors [13].

Prof. Niu [10], [14] from Wuhan University consider magnetic map technology as an important patchwork for autonomous localization in GNSS denied conditions, and have investigated the topology matching localization technology based on smartphones. It is worth mentioning that, our team from Xidian University have carried out various matching

Received 23 October 2024; accepted 25 November 2024. Date of publication 27 November 2024; date of current version 26 March 2025. This work was supported in part by the National Natural Science Foundation of China under Grant 62101399, Grant 62288101, and Grant 62276203; in part by the Open Fund for the Key Laboratory of Inertial Technology under Grant KFJJ-2023-004; in part by the Open Fund of the State Key Laboratory of Satellite Navigation System and Equipment Technology under Grant CEPNT2022B08; in part by the China Post-Doctoral Science Foundation under Grant 2021M692497; in part by the Joint Fund of Shanghai Jiaotong University-Xidian University Key Laboratory of Ministry of Education under Grant LHJJ/2024-9. (Corresponding authors: Gongxu Liu; Long Li.)

Gongxu Liu, Haojie Fan, and Long Li are with the Key Laboratory of High Speed Circuit Design and EMC of Ministry of Education and the School of Electronic Engineering, Xidian University, Xi'an 710071, China (e-mail: liugongxu@xidian.edu.cn; lilong@mail.xidian.edu.cn).

Yang Ji is with the Beijing Automation Control Equipment Research Institute, Beijing 100074, China.

Lu Huang is with the State Key Laboratory of Satellite Navigation System and Equipment Technology, Shijiazhuang 050081, China.

Digital Object Identifier 10.1109/JIOT.2024.3507826

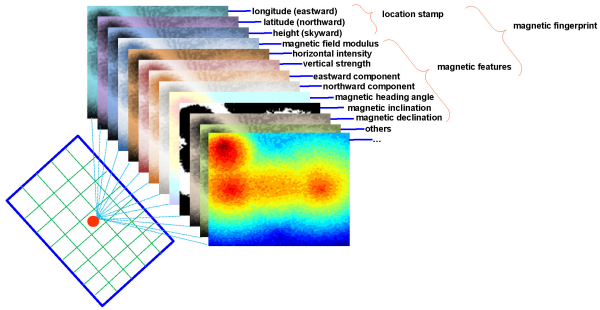


Fig. 1. Basic concept of magnetic map.

localization methods based on magnetic maps, such as the focused matching method [9], AOFA-PF [15], integrated PF [16], etc.

In recent years, the rise of deep learning technologies has a significant impact on magnetic map construction and matching localization [17]. The typical work are as follows. Lee and Han [18] proposed a deep neural network (DNN) to classify magnetic landmarks with known positions to infer the user's location. Adege et al. [19] proposed a hybrid of support vector machine (SVM) and DNN to develop scalable and accurate matching technology. Khan et al. [20] estimated the magnetic field using the deep learning method, which builds a bridge between the data and the model of magnetic map. Finally, it is worth emphasizing that although simultaneous localization and mapping (SLAM) methods and the graph theory derived from machine vision have also been introduced into magnetic map matching localization, the current magnetic map SLAM technology is still in the preliminary research stage and has not yet yielded the expected matching results. In summary, one of the significant challenges of magnetic map matching localization technology is the nonlightweight nature or high computational complexity of the matching architecture, which severely limits the application requirements for high update frequencies or fast-moving targets.

Indeed, magnetometer streaming data at any moment only capture measurements along one direction in space, unlike 2-D image matching where features across an entire plane can be captured and processed simultaneously. Particularly when using only magnetic field modulus as the fingerprint, the measurement information is significantly limited, posing substantial difficulties for matching localization. To tackle these challenges, three main approaches are typically considered. First, longer magnetometer streaming data can provide richer sequence information for more accurate matching but result in prolonged measurement times and reduced efficiency, unsuitable for rapid or real-time applications [21], [22]. Second, obtaining magnetometer streaming data along multiple measurement paths offers more diverse fingerprint information without requiring lengthy sequences. However, this necessitates multiple sensors or complex magnetic sensor arrays, increasing hardware costs and demanding additional efforts to mitigate interference among array elements [23], [24]. Finally, integrating multisensor fusion, specifically combining magnetic maps with inertial navigation systems [25], [26], [27], leverages pose estimates from inertial sensors to offset

the shortcomings of single magnetometer streaming data. This approach achieves a robust matching framework constrained by multiple factors, which is precisely the architecture adopted in this work.

Based on the aforementioned challenges analysis, this article introduces a streamlined, efficient framework for matching localization that integrates magnetic map with inertial sensors. Overall, this article contributes in the following aspects.

First, this article expands the binary framework of magnetic maps, traditionally divided between offline mapping and online matching localization, into a ternary architecture encompassing coarse mapping, fine reconstruction, and matching localization. During the fine reconstruction stage, we re-examine and re-explore the features of the magnetic map, culminating in the derivation of the Bayesian probability integral table (BPIT) under Gaussian modeling. The introduction of BPIT circumvents extensive integration calculations, markedly reducing the computational complexity during the matching localization phase. Second, we proposed the adaptive integrated particle filter (AIPF) for matching localization based on magnetic map and inertial sensors, and the search bounds in the BPIT are adaptively adjusted based on the heading and step length obtained from inertial sensors. Finally, the experimental results under different scenarios demonstrate exponential increase in the efficiency of online matching localization, and the proposed architecture also exhibits excellent resistance to Gaussian related noise.

The remainder of this article is organized as follows. Section II provides a comprehensive description of the lightweight matching positioning architecture based on magnetic maps and inertial sensors. After that, the experimental result and discussion are given in Section III. Finally, Section IV summarizes the conclusion.

II. DESIGN PROCESS OF LIGHTWEIGHT MATCHING LOCALIZATION ARCHITECTURE

The lightweight matching localization architecture based on magnetic maps and inertial sensors is shown in Fig. 2. The magnetic map is constructed through the spatial topological connection of individual magnetic node with specific fingerprint, including location stamp and magnetic feature. There are two reasons for considering only the magnetic field modulus as magnetic fingerprint here. On the one hand, the magnetic map with single kind of fingerprint is relatively easier to construct and more accessible. On the other hand, the single kind of fingerprint is more challenging and more capable of testing the performance of the matching localization methods compared to matching multiple kinds of fingerprints.

A. Reconstruction of Magnetic Map

In order to obtain magnetic maps with fine granularity, Gaussian process regression (GPR) is employed for spatial interpolation [28]. The fundamental idea of GPR is to treat the dataset as a multivariate Gaussian distribution, and then utilize prior knowledge and observed data to construct a posterior Gaussian process (GP) model, thereby estimating and inferring unknown data. According to the principles of

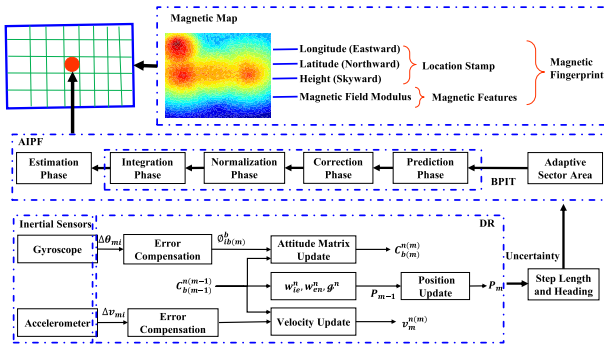


Fig. 2. Lightweight matching localization architecture based on magnetic maps and inertial sensors.

the method described above, we can discretize the constructed magnetic map into several magnetic nodes in advance. Then, these magnetic nodes are divided into sampling points and interpolation points. By collecting magnetic field data from all sampling points, we can construct a posterior GP model that estimates and infers various interpolation points. This achieves spatial interpolation and improves the precision of mapping.

The principle of GPR can be represented by the following mathematical formula: suppose there is a dataset $\mathcal{D} = (x_i, y_i)_{i=1}^n$, where $x_i \in R^d$ represents the input variables, $y_i \in R$ represents the output variables, and n is the size of the dataset. Assuming the output variables y_i can be represented by an unknown function $f(x_i)$ plus Gaussian noise $\epsilon_i \sim N(0, \sigma_n^2)$, i.e.,

$$y_i = f(x_i) + \epsilon_i. \quad (1)$$

Suppose the function $f(x)$ is a GP, which means that for any set of input variables x_1, x_2, \dots, x_n , the corresponding output variables $f(x_1), f(x_2), \dots, f(x_n)$ follow a multivariate Gaussian distribution. A GP can be defined using a mean function $m(x)$ and a covariance function $k(x, x')$, as follows:

$$f(x) \sim GP(m(x), k(x, x')). \quad (2)$$

where

$$m(x) = \mathbb{E}[f(x)] \quad (3)$$

$$k(x, x') = \mathbb{E}[(f(x) - m(x))(f(x') - m(x'))]. \quad (4)$$

The mean function $m(x)$ describes the expected value of the function $f(x)$, which can typically be simplified to zero or a constant. The covariance function $k(x, x')$ describes the correlation between two outputs of the function $f(x)$ and $f(x')$. Commonly used kernel functions, such as the linear kernel, polynomial kernel, and Gaussian kernel can be chosen for this purpose. This article utilizes the Gaussian kernel as the covariance function, expressed as

$$k(x, x') = \sigma_f^2 \exp\left(-\frac{|x - x'|^2}{2l^2}\right) + \sigma_n^2 \delta_{x,x'} \quad (5)$$

where σ_f^2 is the signal variance, l is the length scale, σ_n^2 is the noise variance, and $\delta_{x,x'}$ equals 1 when $x = x'$ and 0 otherwise. These parameters can be estimated through the

marginal likelihood function. The negative logarithm of the likelihood function is often chosen as follows:

$$\begin{aligned} \mathcal{L}(\theta) = -\log p(y | \theta, \mathcal{D}) &= \frac{3}{2} \log |K_\theta + \sigma_{\text{noise}}^2 I_n| \\ &+ \frac{1}{2} \text{tr} \left[y \left(K_\theta + \sigma_{\text{noise}}^2 I_n \right)^{-1} y^\top \right] + \frac{3n}{2} \log(2\pi). \end{aligned} \quad (6)$$

Simultaneously, this article employs the Broyden Fletcher Goldfarb Shanno (BFGS) optimization method to optimize the hyperparameters in GPR, such as the length scale, signal variance, and noise variance. These hyperparameters can be estimated by maximizing the marginal likelihood function, and the BFGS optimization method can quickly find the maximum point of the marginal likelihood function. The BFGS optimization method is an iterative algorithm for solving unconstrained optimization problems. It preprocesses the gradient with curvature information to determine the descent direction and maintains an approximation of the Hessian matrix of the objective function using a generalized secant method to obtain curvature information. The BFGS method has good numerical performance and fast convergence, thus it can be applied to GPR for optimizing the hyperparameters of the kernel function.

The negative logarithm of the likelihood function is used as the objective function optimization. This function represents the entropy of the target value vector given the training data and hyperparameters. It is a convex function, and its minimum value corresponds to the optimal hyperparameters that maximize the marginal likelihood function. Then, the BFGS method is used to solve for the optimal hyperparameters (θ). The update formula of the BFGS method is as follows:

$$B_{k+1} = B_k + \frac{y_k y_k^T}{y_k^T s_k} - \frac{B_k s_k s_k^T B_k^T}{s_k^T B_k s_k} \quad (7)$$

where $s_k = x_{k+1} - x_k$, $y_k = g_{k+1} - g_k$, and $g_k = -\nabla L(x_k)$.

Using the optimal hyperparameters $\hat{\theta}$, we predict the test data to obtain the predicted mean and variance

$$\begin{aligned} \mu* &= m(x*) + k*^T \left(K + \sigma_n^2 I \right)^{-1} (y - m) \\ \sigma*^2 &= k(x*, x*) - k*^T \left(K + \sigma_n^2 I \right)^{-1} k* \end{aligned} \quad (8)$$

where $y = (y_1, y_2, \dots, y_n)^T$ is the vector of output variables, $m = (m(x_1), m(x_2), \dots, m(x_n))^T$ is the vector of mean functions, $k* = (k(x*, x_1), k(x*, x_2), \dots, k(x*, x_n))^T$ is the vector of covariance functions, K is the covariance matrix, and its elements are $K_{ij} = k(x_i, x_j)$. The objective of GPR is to predict an output $f*$ for a new input $x*$ based on the training dataset $\mathcal{D} = (x_i, y_i)_{i=1}^n$.

With the above formula, we can obtain the mean and variance of the output $f*$ for the test input $x*$, thus making predictions and estimations.

Obviously, the disadvantage of GPR is the relatively high computational complexity because of solving large-scale matrix operations and inversions. However, GPR can predict complex data, such as nonlinear, high-dimensional, and sparse data, and to provide uncertainty in the predicted results. GPR is suitable for refining and reconstructing the original

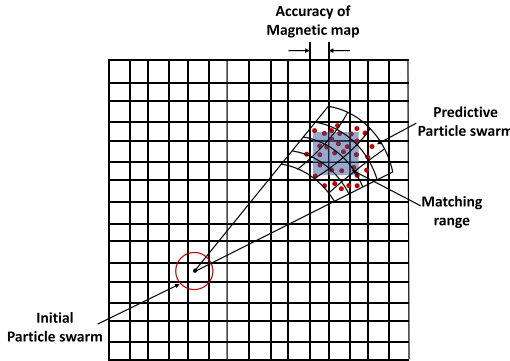


Fig. 3. Distribution and prediction of particles in magnetic map.

magnetic map, which will facilitate the following matching localization.

B. Matching Localization Based on Magnetic Map

The traditional matching localization architecture is based on PF and DR. Here, we proposed the AIPF method based on our previous work [9], [13], [15], [16], and the particle state transition is determined according to the DR motion model, as shown in

$$\begin{aligned} x_{k+1}^i &= x_k^i + (l_k + \Delta l) \times \cos(\theta_k + \Delta\theta) \\ y_{k+1}^i &= y_k^i + (l_k + \Delta l) \times \sin(\theta_k + \Delta\theta) \end{aligned} \quad (9)$$

where x_k^i and y_k^i are the coordinates of the i th particle at step k , and l_k and θ_k are the step length and heading at step k . Since each particle's step length and heading follow a Gaussian distribution, the step length and heading of each particle are different.

The distribution of particles after state transition is shown in Fig. 3. Due to the limitations of magnetic map construction accuracy, the fingerprints in the magnetic map are not continuous. Therefore, in the correction phase of the particle filter, the particles in the blue area use the same fingerprint for weight update. Thus, when the number of particles approaches infinity, the effect of particles in the blue area is equivalent to an integrated particle. The integrated particle is

$$\begin{aligned} P &= [\hat{x}, \hat{y}] \\ \hat{x} &= \int_{x_1}^{x_2} \int_{y_1}^{y_2} x f_{xy}(x, y) dy dx \\ \hat{y} &= \int_{x_1}^{x_2} \int_{y_1}^{y_2} y f_{xy}(x, y) dy dx \end{aligned} \quad (10)$$

where x_1 and x_2 are the lower and upper boundaries of the blue area on the x -axis, respectively, and y_1 and y_2 are the lower and upper boundaries of the blue area on the y -axis, respectively. $f_{xy}(x, y)$ is the probability density of the particles within the blue area

$$w' = \int_{x_1}^{x_2} \int_{y_1}^{y_2} f_{xy}(x, y) dy dx. \quad (11)$$

As shown in Fig. 3, based on the DR motion model equation, the predicted area for the particles is a sector-shaped region. Since it is challenging to integrate particles

with the same fingerprint in the predicted region, we divide the predicted particles into smaller sector-shaped regions for integration. After particle integration, we can match the equivalent fingerprint in the same sector-shaped region of the magnetic map. The smaller the sector-shaped regions are divided, the higher the overall accuracy of matching particles with the true fingerprints, and the better it fits the system's posterior probability density.

Let $l \sim N(l_0, \sigma_1)$ and $\theta \sim N(\theta_0, \sigma_2)$, where the heading and step length in the motion model are independent. Therefore, the weight of the integrated particles in the sector-shaped region is

$$\begin{aligned} w &= \int_{\theta_1}^{\theta_2} \int_{l_1}^{l_2} f_{\theta l}(\theta, l) d\theta dl \\ &= \int_{l_1}^{l_2} f_l dl \int_{\theta_1}^{\theta_2} f_\theta d\theta \\ &= \int_{l_1}^{l_2} \frac{1}{\sqrt{2\pi}\sigma_1} e^{-\frac{(l-l_0)^2}{2\sigma_1^2}} dl \int_{\theta_1}^{\theta_2} \frac{1}{\sqrt{2\pi}\sigma_2} e^{-\frac{(\theta-\theta_0)^2}{2\sigma_2^2}} d\theta. \end{aligned} \quad (12)$$

The expected step length within the sector-shaped region is

$$\begin{aligned} \hat{l} &= \int_{\theta_1}^{\theta_2} \int_{l_1}^{l_2} l f_{\theta l}(\theta, l) d\theta dl \\ &= \frac{\int_{l_1}^{l_2} l \frac{1}{\sqrt{2\pi}\sigma_1} e^{-\frac{(l-l_0)^2}{2\sigma_1^2}} dl \int_{\theta_1}^{\theta_2} \frac{1}{\sqrt{2\pi}\sigma_2} e^{-\frac{(\theta-\theta_0)^2}{2\sigma_2^2}} d\theta}{w}. \end{aligned} \quad (13)$$

Similarly, the expected heading within the sector-shaped region is

$$\begin{aligned} \hat{\theta} &= \int_{\theta_1}^{\theta_2} \int_{l_1}^{l_2} \theta f_{\theta l}(\theta, l) d\theta dl \\ &= \frac{\int_{l_1}^{l_2} \frac{1}{\sqrt{2\pi}\sigma_1} e^{-\frac{(l-l_0)^2}{2\sigma_1^2}} dl \int_{\theta_1}^{\theta_2} \theta \frac{1}{\sqrt{2\pi}\sigma_2} e^{-\frac{(\theta-\theta_0)^2}{2\sigma_2^2}} d\theta}{w}. \end{aligned} \quad (14)$$

The particles integrated from the sector area are

$$\begin{aligned} \hat{x} &= x_k + \hat{l} \cdot \cos \hat{\theta} \\ \hat{y} &= y_k + \hat{l} \cdot \sin \hat{\theta} \\ P &= [\hat{x}, \hat{y}]. \end{aligned} \quad (15)$$

It is important to note that in (12) and (13), the calculation of probabilities and expectations for l and θ within the given region requires integration. However, integration is a computationally expensive operation. Therefore, we optimize the computation using properties of the Gaussian distribution to improve the speed of calculations. The specific method is as follows:

Since $l \sim N(l_0, \sigma_1)$ and $\theta \sim N(\theta_0, \sigma_2)$, according to the properties of the normal distribution, we have

$$\begin{aligned} \frac{l - l_0}{\sigma_1} &\sim N(0, 1) \\ \frac{\theta - \theta_0}{\sigma_2} &\sim N(0, 1). \end{aligned} \quad (16)$$

Therefore, (12) to (14) can be transformed by linearly transforming the probabilities and expectations within the

standard normal distribution region. The transformed equation (12) is

$$\begin{aligned} w &= \int_{l_1}^{l_2} \frac{1}{\sqrt{2\pi}\sigma_1} e^{-\frac{(l-l_0)^2}{2\sigma_1^2}} dl \int_{\theta_1}^{\theta_2} \frac{1}{\sqrt{2\pi}\sigma_2} e^{-\frac{(\theta-\theta_0)^2}{2\sigma_2^2}} d\theta \\ &= \int_{\frac{l_1-l_0}{\sigma_1}}^{\frac{l_2-l_0}{\sigma_1}} \frac{1}{\sqrt{2\pi}} e^{-\frac{l^2}{2}} dl \int_{\frac{\theta_1-\theta_0}{\sigma_2}}^{\frac{\theta_2-\theta_0}{\sigma_2}} \frac{1}{\sqrt{2\pi}} e^{-\frac{\theta^2}{2}} d\theta. \end{aligned} \quad (17)$$

The transformed equation (13) is as follows:

$$\hat{l} = \frac{\sigma_1 \int_{\frac{l_1-l_0}{\sigma_1}}^{\frac{l_2-l_0}{\sigma_1}} l \frac{1}{\sqrt{2\pi}} e^{-\frac{l^2}{2}} dl + l_0 \int_{\frac{l_1-l_0}{\sigma_1}}^{\frac{l_2-l_0}{\sigma_1}} \frac{1}{\sqrt{2\pi}} e^{-\frac{l^2}{2}} dl}{\sigma_1 \int_{\frac{l_1-l_0}{\sigma_1}}^{\frac{l_2-l_0}{\sigma_1}} \frac{1}{\sqrt{2\pi}} e^{-\frac{l^2}{2}} dl}. \quad (18)$$

Similarly, the transformed equation (14) is as follows:

$$\hat{\theta} = \frac{\sigma_2 \int_{\frac{\theta_1-\theta_0}{\sigma_2}}^{\frac{\theta_2-\theta_0}{\sigma_2}} \theta \frac{1}{\sqrt{2\pi}} e^{-\frac{\theta^2}{2}} d\theta + \theta_0 \int_{\frac{\theta_1-\theta_0}{\sigma_2}}^{\frac{\theta_2-\theta_0}{\sigma_2}} \frac{1}{\sqrt{2\pi}} e^{-\frac{\theta^2}{2}} d\theta}{\int_{\frac{\theta_1-\theta_0}{\sigma_2}}^{\frac{\theta_2-\theta_0}{\sigma_2}} \frac{1}{\sqrt{2\pi}} e^{-\frac{\theta^2}{2}} d\theta}. \quad (19)$$

After the transformation, we can pre-establish a BPIT based on the standard normal distribution probability function $F(x)$ and expectation function $G(x)$. Thus, the integration steps can be eliminated by directly querying the integral results from the BPIT. This significantly improves computational efficiency. The probability function $F(x)$ and expectation function $G(x)$ are

$$\begin{aligned} F(x) &= \int_{-\infty}^x f(t) dt \\ G(x) &= \int_{-\infty}^x tf(t) dt \end{aligned} \quad (20)$$

where $f(t)$ is the probability density function of the standard normal distribution, therefore, the results of (17)–(19) are obtained by querying $F(x)$ and $G(x)$. Equations (17)–(19) are transformed as follows:

$$w = \left[F\left(\frac{l_2-l_0}{\sigma_1}\right) - F\left(\frac{l_1-l_0}{\sigma_1}\right) \right] \left[F\left(\frac{\theta_2-\theta_0}{\sigma_2}\right) - F\left(\frac{\theta_1-\theta_0}{\sigma_2}\right) \right] \quad (21)$$

$$\hat{l} = \frac{\sigma_1 \left[G\left(\frac{l_2-l_0}{\sigma_1}\right) - G\left(\frac{l_1-l_0}{\sigma_1}\right) \right] + l_0 \left(F\left(\frac{l_2-l_0}{\sigma_1}\right) - F\left(\frac{l_1-l_0}{\sigma_1}\right) \right)}{F\left(\frac{l_2-l_0}{\sigma_1}\right) - F\left(\frac{l_1-l_0}{\sigma_1}\right)} \quad (22)$$

$$\hat{\theta} = \frac{\sigma_2 \left[G\left(\frac{\theta_2-\theta_0}{\sigma_2}\right) - G\left(\frac{\theta_1-\theta_0}{\sigma_2}\right) \right] + \theta_0 \left[F\left(\frac{\theta_2-\theta_0}{\sigma_2}\right) - F\left(\frac{\theta_1-\theta_0}{\sigma_2}\right) \right]}{F\left(\frac{\theta_2-\theta_0}{\sigma_2}\right) - F\left(\frac{\theta_1-\theta_0}{\sigma_2}\right)}. \quad (23)$$

Establishing the BPIT based on the probability function $F(x)$ and expectation function $G(x)$ of the standard normal distribution takes dozens of minutes, and it can be reused in the matching localization. In a way, BPIT is a deep processing of magnetic map features under some kind of the noise model, which can greatly accelerate the matching localization process.

Combined with the DR motion model based on inertial sensors, the predicted particle distribution is determined by the sector region determined by the heading and step length.

Assuming that all kinds of noise can always consist of Gaussian white noise, we utilize the 3σ principle of the Gaussian distribution: the probability of a numerical value lying within the interval $[u - 3\sigma, u + 3\sigma]$ is 0.9974. Hence, the predicted particle distribution region is determined by

$$\begin{cases} \theta \in [\theta_0 - 3\sigma_2, \theta_0 + 3\sigma_2] \\ l \in [l_0 - 3\sigma_1, l_0 + 3\sigma_1]. \end{cases} \quad (24)$$

Assuming that all initial particles are in the same position undoubtedly reduces the diversity of particles. Therefore, we compensate for σ_1 and σ_2 to make up for the loss of particle diversity. The specific measure is as follows: we superimpose the root mean square of step length and heading from the previous PF results onto the new PF process. At the same time, we set two thresholds to prevent the convergence of heading and step length, which could lead to the loss of particle diversity. The values of σ_1 and σ_2 are

$$\begin{cases} \sigma_1 = \max(\sigma_l + \sigma_{\Sigma l}, \sigma_{lh}) \\ \sigma_2 = \max(\sigma_\theta + \sigma_{\Sigma \theta}, \sigma_{\theta h}) \end{cases} \quad (25)$$

where σ_l represents the uncertainty in step length calculated by the inertial sensors, and we take $\sigma_l = 0.1l$, $\sigma_{\Sigma l}$ represents the root mean square of step length from the previous filtering result, σ_θ is the uncertainty in heading estimated, and $\sigma_{\Sigma \theta}$ is the root mean square of heading from the previous filtering results. σ_{lh} and $\sigma_{\theta h}$ are the threshold values set for step length and heading uncertainty, respectively.

In Fig. 3, we can observe that the small sectors covering the matched area of magnetic map nodes (i.e., the blue area) can be divided into two types: 1) those completely within the blue area and 2) those partially within the blue area. Among the sectors completely within the blue area, particles can match with correct fingerprints, while particles partially within the blue area may match with incorrect fingerprints, and the matching accuracy is related to the area of the blue or white regions within the sector. Obviously, the smaller the subdivided integration area, the higher the overall matching accuracy, but there will always be an inherent error due to the incomplete overlap of the blue and white areas. We use feature length as the basis for dividing the sector regions, specifically by ensuring that the lengths of each side of the divided regions are smaller than the feature length

$$\begin{aligned} n &= 1 \\ d &= \frac{\text{Map Accuracy}}{n} \\ n1 &= \frac{6\sigma_1}{d} \\ n2 &= \frac{6\sigma_2(l_0 + 3\sigma_1)}{d} \end{aligned} \quad (26)$$

where d is the feature length, which is $(1/n)$ times the accuracy of the magnetic map, and $n1$ and $n2$ are the numbers of divisions for the step length and heading edges, respectively.

A common method for positioning using measured magnetic field strength is to use a statistical model. When the magnetic field measurement error follows a Gaussian distribution, the

likelihood function is given by a multivariate normal distribution with mean $h(\mathbf{x})$ and covariance \mathbf{R}

$$p(z | \mathbf{x}) = \frac{1}{\sqrt{(2\pi)^n |\mathbf{R}|}} \exp\left(-\frac{1}{2}(z - h(\mathbf{x}))^T \mathbf{R}^{-1} (z - h(\mathbf{x}))\right) \quad (27)$$

where z is the measurement value of the magnetic field, \mathbf{x} is the position, $h(\mathbf{x})$ is the magnetic fingerprint at position \mathbf{x} in the magnetic map, and n is the dimensionality of the magnetic field vector z . If the modulus of the magnetic field strength is used as the measurement value, the multivariate normal distribution will degenerate into a univariate normal distribution. In this stage, (27) is used to update the weights of integrated particles. After the update, the weights of the integrated particles are

$$w = w^* \frac{1}{\sqrt{(2\pi)^n |\mathbf{R}|}} \exp\left(-\frac{1}{2}(z - h(\mathbf{x}))^T \mathbf{R}^{-1} (z - h(\mathbf{x}))\right). \quad (28)$$

In a word, the AIPF process can be summarized as follows.

- 1) *Prediction Phase*: The prediction stage determines the sector region based on the uncertainty of heading and step length.
- 2) *Correction Phase*: Update the weights of integrated particles based on fingerprint information in the magnetic map.
- 3) Normalization phase.
- 4) *Integration Phase*: Divide small sector regions and integrate particles within these regions.
- 5) Estimation phase.
- 6) Repeat steps a–e.

III. EXPERIMENTAL VERIFICATION AND DISCUSSION

Three state-of-the-art matching methods, including PF, the adaptive optimization firefly algorithm (AOFA), and extended Kalman particle filter (EKPF) are used to compare the performance of the proposed algorithm. The number of particles is set to 1000.

A. Matching Localization Assessment by Magnetic Map Based on IGRF Model

The IGRF model primarily describes Earth's dominant magnetic field [29], encompassing core-generated and external influences. The Earth magnetic anomaly grid (two-arc-minute resolution) (EMAG2) focuses more on mapping the magnetic structures of the crust and upper mantle. In practice, scientists and engineers often utilize both EMAG2 and the IGRF model together. For instance, in navigation, accounting for magnetic anomalies while referencing precise field data from the IGRF model may be necessary.

The magnetic map data employed here was produced through software developed by our team, based on the IGRF model with considerations given to local magnetic distortion sources (<https://github.com/XDU-GXL/Magnetic-Map>).

1) *Matching Localization Comparison Under Different Trajectories*: We set three types of paths, and calculate the trajectory matrices of the paths, as well as matrices of step lengths and headings, as necessary input for subsequent

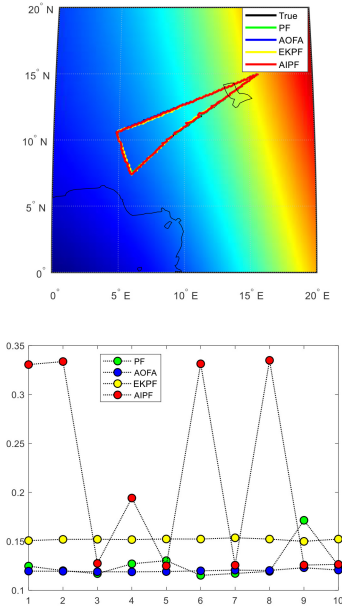


Fig. 4. Results of various algorithms for Trajectory 1.

TABLE I
COMPREHENSIVE ANALYSIS OF TEN EXPERIMENTS ON TRAJECTORY 1

Method	Mean RMSE	Mean Average Error	Mean Computation Time (Second)
PF	1.19586	1.29853	2.9116
AOFA	1.15263	1.15012	3.7815
EKPF	1.41079	1.40623	1.8420
AIPF	1.23323	1.68002	0.0842

matching localization. Contrasting experiments with multiple paths can better reflect the computational conditions of each algorithm when processing different trajectories.

For each individual experiment, the root mean-square error (RMSE) and mean error are selected as evaluation indicators. Due to the randomness of single experiment data, repeated experiments ten times for each trajectory using different algorithms, and all experimental data results are saved for analysis. Sometimes, the dimensional matching outcomes prove deficient in offering meaningful benchmarks. The ratio of matching localization error to the original magnetic map's granularity represents as a dimensionless evaluation metric and holds greater relevance across the different reference magnetic maps.

As shown in Fig. 4 and Table I, for the repeated ten experiments of Trajectory 1, the matching localization accuracy of the AIPF method is comparable or slightly degraded compared to the state-of-the-art methods. Taking the mean RMSE metric as an example, the proposed method shows a relative performance decrease of 3%, a decrease of 7%, and an improvement of 14% compared to PF, AOFA, and EKPF. However, the AIPF method requires only 0.0842 s of the computational time, which is 2.9%, 2.2%, and 4.6% of the computation time of PF, AOFA, and EKPF.

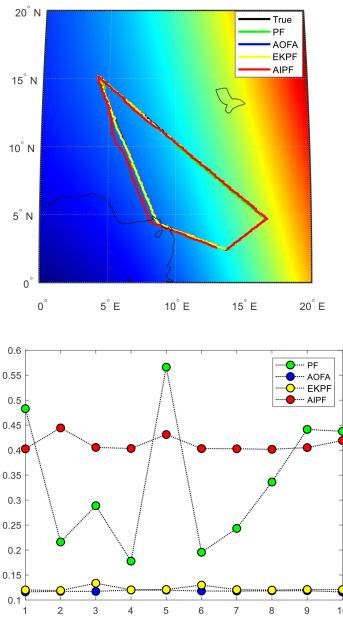


Fig. 5. Results of various algorithms for Trajectory 2.

TABLE II
COMPREHENSIVE ANALYSIS OF TEN EXPERIMENTS ON TRAJECTORY 2

Methods	Mean RMSE	Mean Average Error	Mean Computation Time (Second)
PF	2.70018	2.96229	3.9250
AOFA	1.16115	1.13084	5.0095
EKPF	1.22348	1.14494	2.4329
AIPF	1.69875	2.36507	0.1100

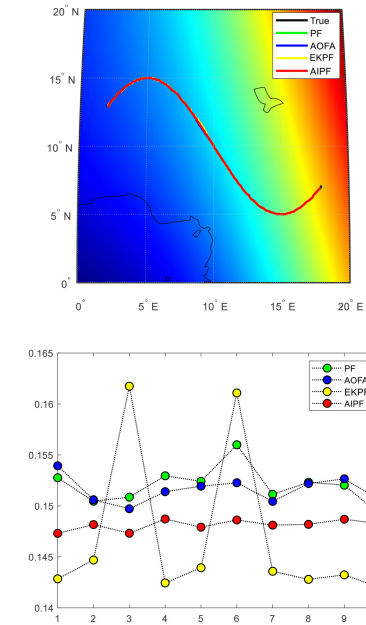


Fig. 6. Results of various algorithms for Trajectory 3.

TABLE III
COMPREHENSIVE ANALYSIS OF TEN EXPERIMENTS ON TRAJECTORY 3

Methods	Mean RMSE	Mean Average Error	Mean Computation Time (Second)
PF	1.47375	1.47234	1.6870
AOFA	1.44414	1.44741	2.1746
EKPF	1.38752	1.39541	1.0506
AIPF	1.43507	1.43309	0.0463

The repeated ten experiments of Trajectory 2 is shown in Fig. 5 and Table II. Taking the mean RMSE metric as an example, the proposed method shows a relative performance improvement of 59%, a decrease of 46%, and a decrease of 39% compared to PF, AOFA, and EKPF. However, the AIPF method requires only 0.11 s of the computational time, which is 3%, 2.2%, and 4.5% of the computation time of PF, AOFA, and EKPF.

In the comprehensive analysis of the ten experiments on Trajectory 3, the EKPF method exhibits the best matching accuracy, while the other three methods achieve similar levels of accuracy. However, the AIPF method only requires 0.0463 computation time, indicating an optimization level of over 20 times in terms of processing efficiency. As shown in Fig. 6 and Table III, for the repeated ten experiments of Trajectory 3, the matching localization accuracy of the AIPF method is comparable to the state-of-the-art methods. Taking the mean RMSE metric as an example, the proposed method shows a relative performance improvement of 2.7%, an improvement of 0.6%, and a decrease of 3.4% compared to PF, AOFA, and EKPF. However, the AIPF method requires only 0.0463 s of the computational time, which is 2.7%, 2.1%, and 4.4% of the computation time of PF, AOFA, and EKPF.

2) *Impact of Magnetic Measurement Noise on Matching Localization:* In real-world environments, magnetic data

collection inevitably accompanies various sources of interference. Here, we uniformly characterize using uncertainty, which is dimensionless evaluation metric after normalization of various types of noise or interference.

The theoretical magnetic values obtained through sampling devices are the result of the superposition of multiple sources of interference at a certain moment and position coordinate in the magnetic field. To simulate the phenomenon of multiple interference sources affecting the magnetic field in a real environment, we can set interference sources to simulate this superposition interference phenomenon. According to the central limit theorem, the superposition of multiple interference sources tends to follow a Gaussian distribution in the limit. Therefore, in this experiment, we add Gaussian noise of different intensity factors to the constructed magnetic map to simulate the effect of interference. After adding Gaussian white noise with different intensity factors, we obtain the result as shown in Fig. 7 (uncertainty is 5) and Fig. 8 (uncertainty is 10).

By introducing Gaussian white noise of different uncertainty into the magnetic map and conducting matching localization experiments, each set of experiments was repeated ten times to obtain the average results, as shown in Table IV. The results show as follows.

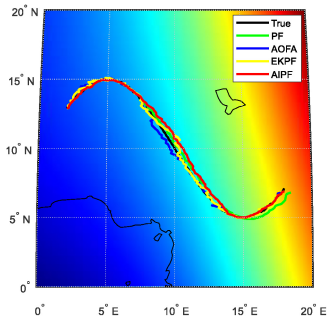


Fig. 7. Comparison of matching trajectories for each algorithm.

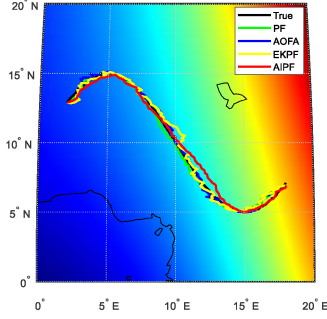


Fig. 8. Comparison of matching trajectories for each algorithm with uncertainty 10.

TABLE IV

DIFFERENT INTENSITY FACTORS FOR REPEATED TEN EXPERIMENTS AND THE MATCHING RESULTS OF EACH METHOD

Uncertainty	Mean RMSE			
	PF	AOFA	EKF	AIPF
1	1.51742	1.60490	1.58203	1.48657
5	5.44013	2.55032	2.70689	3.56745
10	6.10836	6.33786	4.87292	4.90103
20	11.25558	23.07308	9.94811	8.23293

When the uncertainty is 1, the proposed method shows a relative performance improvement of 2.1%, an improvement of 8%, and an improvement of 6.4% compared to PF, AOFA, and EKPF.

When the uncertainty is 5, the proposed method shows a relative performance improvement of 52.5%, a decrease of 39.9%, and a decrease of 31.8% compared to PF, AOFA, and EKPF.

When the uncertainty is 10, the proposed method shows a relative performance improvement of 24.6%, an improvement of 29.3%, and a decrease of 0.6% compared to PF, AOFA, and EKPF.

When the uncertainty is 20, the proposed method shows a relative performance improvement of 36.7%, an improvement of 280%, and an improvement of 20.8% compared to PF, AOFA, and EKPF.

In summary, the proposed method is less affected by the increase in noise compared to the other three methods.

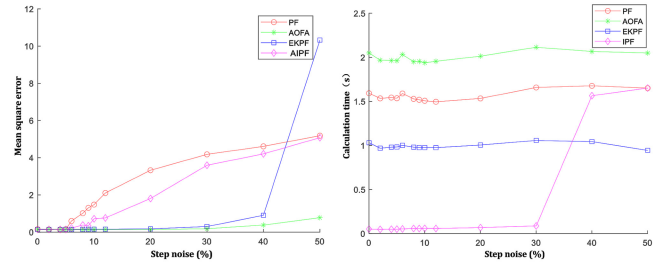


Fig. 9. Effect of step length uncertainly on output results.

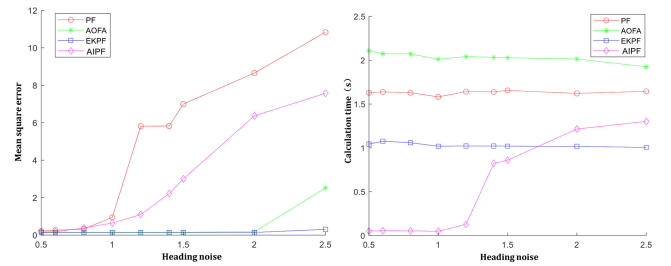


Fig. 10. Effect of heading uncertainly on output results.

3) Effect of Step Length and Heading Uncertainty on Matching Localization: To simulate the errors of inertial sensors data, we add step length and heading uncertainty when matching localization. Subsequently, the magnetic map matching trajectory results output by the four algorithms are compared and analyzed.

Based on the above experiments, it can be concluded that when the heading noise is less than 1.2 degrees or the step length noise is less than 30% of the precision of reference magnetic map, the AIPF method can achieve comparable accuracy with other three methods, while the computation time of the proposed method is only one-tenth of the compared methods. As can be seen in Figs. 9 and 10, the efficiency advantage of the proposed method is lost when the step or heading uncertainty continues to increase. In fact, at this point, the performance of the inertial sensor has deteriorated so badly that it cannot even be used properly either.

B. Matching Localization Assessment on Indoor Magnetic Map

1) Reconstruction of Indoor Magnetic Map: Using GPR for spatial interpolation requires dividing the sampling points into training set and prediction set. Based on the training set, GPR can be used to acquire the prediction set, which are subsequently compared with the actual values. The common proportional relationships between training points and prediction points are 3:1 and 1:1, respectively. The mapping interval between adjacent nodes is set to 0.3 m, which is the precision of the magnetic map. The spatial distribution of training and prediction points for the two interpolation modes is illustrated in Fig. 11, where the blue points represent magnetic nodes used for training, while red points represent magnetic nodes used for prediction.

The testing ground is the corridor on the fourth floor of a dormitory building of Xidian University, as shown in

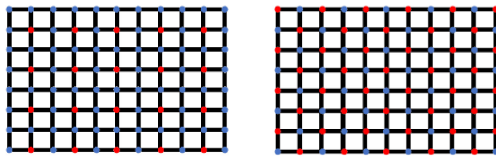


Fig. 11. Comparison of spatial distribution between 3:1 and 1:1 interpolation.



Fig. 12. Using the corridor as a testing ground.

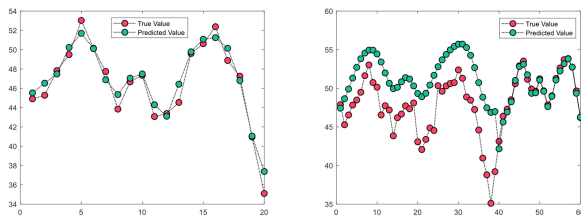


Fig. 13. Comparison between predicted values and GT for 3:1 and 1:1 interpolation.

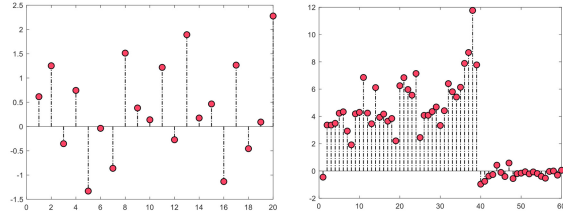


Fig. 14. Comparison of error values between predicted values and GT for 3:1 and 1:1 interpolation.

Fig. 12, with the red line indicating the walking trajectory for subsequent experiments.

A 2-D magnetic map is established at a height of 1.2 m above the ground. Each tile of the corridor floor is with a side length of 60 cm, serving as a magnetic node. The magnetic field modulus at the vertices of each floor tile on the plane is sampled and recorded. Using the two proportional relationships mentioned above to partition the training and prediction groups, the experimental results are shown in Fig. 13, where the green points represent predicted values and the red points represent true values.

The error values for each prediction point are shown in Fig. 14.

The evaluation metrics used in Table V, including the sum of squared errors (SSEs), the mean absolute error (MAE), the mean-squared error (MSE), the RMSE, the mean absolute percentage error (MAPE), and the correlation coefficient (CC).

TABLE V
ERROR SITUATION OF PREDICTED VALUES VERSUS GT FOR TWO INTERPOLATIONS MODES

Mode	SSE (m)	MAE (m)	MSE (m)	RMSE (m)	MAPE (%)	CC
3:1	21.270	0.8238	1.0635	1.0313	1.8371	0.9783
1:1	1096.5	3.2796	18.274	4.2749	7.2525	0.6439

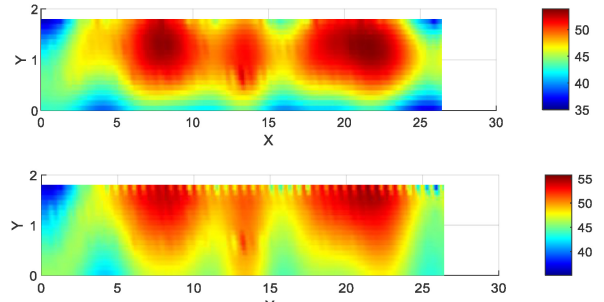


Fig. 15. Magnetic maps constructed under 3:1 and 1:1 interpolation mode.

By combining the magnetic field modulus of the sampling magnetic nodes with that of the interpolation nodes and applying a smoothing process, the magnetic maps constructed under the two modes are shown in Fig. 15.

As shown in Table V, the results show that the 3:1 proportional interpolation mode can predict values better. This demonstrates that using GPR for spatial interpolation in this way can effectively improve the efficiency of offline geomagnetic map construction while ensuring the reliability of interpolation nodes. Although the 1:1 proportional interpolation mode can improve the efficiency, the error between predicted values and true values is significant, indicating insufficient reliability. Therefore, we will select the 3:1 proportional interpolation mode to construct the magnetic map, which will be used to evaluate the compared methods.

2) *Performance Assessment on Matching Localization Methods:* In the corridor environment, data from accelerometers, gyroscopes, and magnetic sensors are collected using handheld smartphones. The fusion navigation technology algorithm based on the ensemble PF method is utilized to compute the pedestrian's walking trajectory. Two experimental modes are carried out, namely straight trajectory and Z-shaped trajectory. The straight trajectory starts from coordinates (0, 1.5) and ends at (12, 1.5), while the Z-shaped walking trajectory starts from coordinates (0, 1.5), turns the right at (6, 1.5), then the left at (6, 0.3), and finally goes straight to the endpoint at (12, 0.3). The results of the experiments for straight trajectory and Z-shaped trajectory are illustrated in Fig. 16, where the yellow line segments represent ground truth (GT) of the walking trajectory.

By recording and calculating the average error of the simulation results for each algorithm over ten runs, the experimental results are shown in Tables VI and VII.

In straight trajectory mode, the proposed method shows a relative performance improvement of 3.9%, an improvement

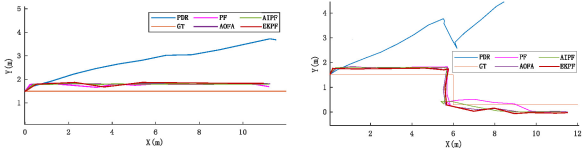


Fig. 16. Error comparison of the four matching localization methods under straight trajectory mode and Z-shaped trajectory mode.

TABLE VI
ERROR SITUATION OF ALGORITHMIC CALCULATIONS FOR
STRAIGHT TRAJECTORY

Methods	Min Error (m)	Max Error (m)	Mean Error (m)	RMSE (m)	Computation Time (Second)
PF	0.3337	1.1946	0.8170	0.8544	0.8375
AOFA	0.2941	1.2780	1.0640	1.0266	1.1374
EKPF	0.2573	0.9528	0.5957	0.7748	0.2185
AIPF	0.2847	0.9389	0.6259	0.8224	0.0796

TABLE VII
ERROR SITUATION OF ALGORITHMIC CALCULATIONS FOR
Z-SHAPED TRAJECTORY

Methods	Min Error (m)	Max Error (m)	Mean Error (m)	RMSE (m)	Computation Time (Second)
PF	0.2716	1.1654	0.5415	0.6055	0.5731
AOFA	0.2927	0.9959	0.5793	0.6216	0.8736
EKPF	0.2849	0.8593	0.4686	0.5374	0.3242
AIPF	0.3009	0.8659	0.4899	0.5270	0.0498

of 24.8%, and a decrease of 6.1% compared to PF, AOFA, and EKPF in terms with the RMSE metric. However, the AIPF method requires only 0.0796 s of the computational time, which is 9.5%, 7.0%, and 36.4% of the computation time of PF, AOFA, and EKPF.

In straight trajectory mode, the proposed method shows a relative performance improvement of 14.9%, an improvement of 18.0%, and an improvement of 2.0% compared to PF, AOFA, and EKPF in terms with the RMSE metric. However, the AIPF method requires only 0.0796 s of the computational time, which is 8.7%, 5.7%, and 15.4% of the computation time of PF, AOFA, and EKPF.

In summary, the real experiments show the AIPF method has comparable localization accuracy while the computational complexity is reduced to one-tenth of that in the compared methods.

C. Matching Localization Assessment on Outdoor Magnetic Map

To better reflect how our algorithm performs within extensive areas characterized by magnetic anomalies, we conducted validations via drones over a coastal region in eastern China, achieving geomagnetic survey precision down to 0.1 Nt. The refined magnetic map precision is 0.001. During experiments, the uncertainty of step length was 0.1 times the magnetic map

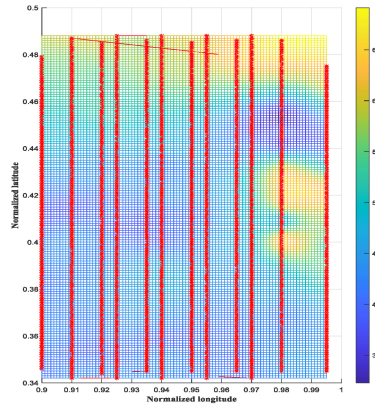


Fig. 17. Measured outdoor magnetic map.

precision, and the uncertainty of heading direction was 0.1° . The dataset spans an area covering dozens of square kilometers in reality. Due to geographical information security concerns, latitude and longitude coordinates have been normalized.

1) *Reconstruction of Outdoor Magnetic Map:* As shown in Fig. 17, the red line denotes the path mapped by the drone, flying at approximately 10 m per second, with magnetic data outputted at a frequency of 5 Hz. Subsequently, the Kriging or V4 interpolation method is applied to refine the magnetic map, which then serves as the reference magnetic map. Unlike the dataset in Section III-A that represents Earth's primary magnetic field, the dataset in Section III-C presents magnetic anomalies. These are the differences between the measured magnetic field and the IGRF main field.

2) *Performance Assessment on Matching Localization Methods:* In the comprehensive analysis of the ten experiments on square-shaped trajectory, the EKPF method exhibits the best matching accuracy, while the other three methods achieve similar levels of accuracy. However, the AIPF method only takes 0.082 computing time, which improves the processing efficiency by more than 20 times at most and 11 times at least. As shown in Figs. 18–20 and Table VIII, for the repeated ten experiments of square-shaped trajectory, the matching localization accuracy of the AIPF method is comparable to the state-of-the-art methods. Taking the mean RMSE metric as an example, the proposed method shows a relative performance decrease of 11.5%, an improvement of 56%, and a decrease of 25% compared to PF, AOFA, and EKPF. However, the AIPF method requires only 0.082 s of the computational time, which is 4.8%, 4.07%, and 8.3% of the computation time of PF, AOFA, and EKPF.

In the comprehensive analysis of the ten experiments on circular trajectory, the EKPF method exhibits the best matching accuracy, while the other three methods achieve similar levels of accuracy. However, the AIPF method only requires 0.0289 computation time, indicating an optimization level of over 20 times in terms of processing efficiency. As shown in Figs. 21–23 and Table IX, for the repeated ten experiments of circular trajectory, the matching localization accuracy of the AIPF method is comparable to the state-of-the-art methods. Taking the mean RMSE metric as an example, the proposed method shows a relative performance improvement of 21%, an

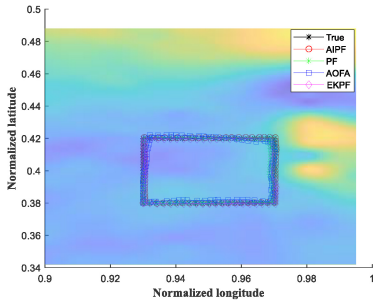


Fig. 18. Visual experimental results along a square-shaped trajectory.

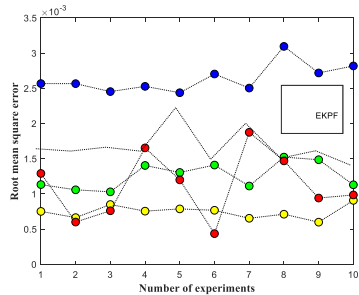


Fig. 19. Each RMSE of ten trials for matching localization using various algorithms under a square-shaped trajectory.

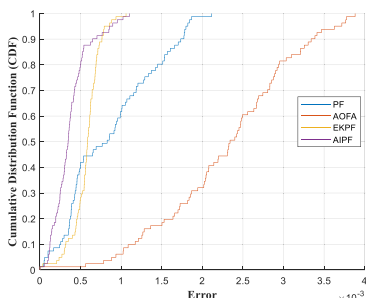


Fig. 20. CDF of matching localization by using various algorithms under a square-shaped trajectory.

improvement of 64%, and a decrease of 20% compared to PF, AOFA, and EKPF. However, the AIPF method requires only 0.0463 s of the computational time, which is 4.1%, 3.4%, and 7% of the computation time of PF, AOFA, and EKPF.

D. Discussion

In Section III-A1 (Fig. 5 and Table II), it is worth mentioning that the difference in relative matching localization accuracy under Trajectory 2 is relatively large, mainly because the test trajectory is long and large segments of the trajectory are in the region where the magnetic fingerprints have almost disappeared, which destroys the assumption applied by the AIPF that the fingerprints or the noise need to satisfy a Gaussian distribution.

Overall, from the experiments mentioned above, it can be observed that the AIPF algorithm sacrifices about 10% of matching accuracy, but it can increase the computational efficiency by approximately ten times. Additionally, the algorithm itself exhibits a certain degree of resistance to magnetic

TABLE VIII
COMPREHENSIVE ANALYSIS OF TEN TRAILS ON
SQUARE-SHAPED TRAJECTORY

Method	Mean RMSE	Mean Average Error	Mean Computation Time (Second)
PF	1.246	1.076	0.6953
AOFA	2783	2.623	0.8313
EKPF	0.813	0.779	0.4124
AIPF	0.976	0.873	0.0289

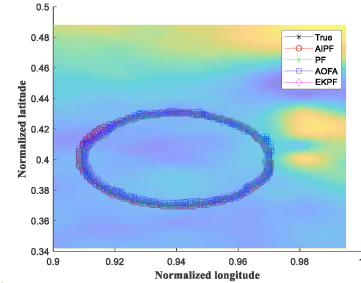


Fig. 21. Visual experimental results along a circular trajectory.

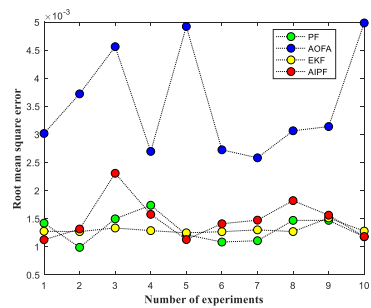


Fig. 22. Each RMSE of ten trials for matching localization using various algorithms under a circular trajectory.

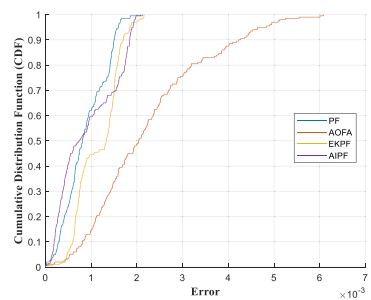


Fig. 23. CDF of matching localization by using various algorithms under a circular trajectory.

map interference, mitigating the impact of step and heading fluctuations.

In this article, we propose a lightweight framework for magnetic map matching localization. This framework builds upon the fusion of particle filter and IMU, it can achieve fast matching localization by substituting complex integral computations during the matching process with BPIT under the Gaussian model. Indeed, Gaussian models are prevalent in natural phenomena. Our collected datasets, covering both

TABLE IX
COMPREHENSIVE ANALYSIS OF TEN EXPERIMENTS ON
CIRCULAR TRAJECTORY

Method	Mean RMSE	Mean Average Error	Mean Computation Time (Second)
PF	1.432	1.274	1.6853
AOFA	3.948	3.240	2.0134
EKPF	1.227	1.134	0.9837
AIPF	1.560	1.421	0.0820

intricate indoor electromagnetic environments and vast outdoor spaces, plus those obtained from global magnetic map, all exhibit Gaussian-distributed magnetic fingerprint patterns. This confirms the validity of our BPIT created on the basis of Gaussian models under common scenarios. For unusually complex magnetic fingerprint distributions or those following nonsingle-Gaussian patterns, a Gaussian mixture model (GMM) serves well. A GMM, consisting of multiple Gaussian probability density functions combined, can simulate any shape of density distribution. Based on practical fingerprint distributions, we can identify the primary Gaussian components in a GMM, calculate their associated BPITs individually, and merge them to form the overall BPIT for the GMM. As a result, our proposed streamlined localization structure easily adapts to magnetic fingerprint datasets modeled by GMMs, with no significant changes required in other aspects.

IV. CONCLUSION

Aiming to address the issue that magnetic map matching localization technology cannot meet the high position update frequency requirements for fast-moving targets, this study investigates a lightweight matching positioning architecture based on magnetic map and inertial sensors. The most significant difference with the existing matching localization methods is that the original magnetic map is not directly utilized in this architecture, but the magnetic features are mined and reconstructed on the basis of the refined magnetic map, and the corresponding BPIT is constructed, so that the accelerated matching localization can be achieved in the proposed AIPF method that contains five phases. The results show the new architecture can significantly enhance the efficiency and robustness of matching localization. In summary, this work provides a new solution for lightweight matching localization algorithms using magnetic maps for variety of challenging positioning and navigation applications.

REFERENCES

- [1] G. He, X. Yuan X, Y. Zhuang, and H. Hu, "An integrated GNSS/LiDAR-SLAM pose estimation framework for large-scale map building in partially GNSS-denied environments," *IEEE Trans. Instrum. Meas.*, vol. 70, pp. 1–9, Sep. 2020.
- [2] A. Canciani and J. Raquet, "Airborne magnetic anomaly navigation," *IEEE Trans. Aerosp. Electron. Syst.*, vol. 53, no. 1, pp. 67–80, Feb. 2017.
- [3] A. Sheinker, B. Ginzburg, N. Salomonski, A. Yaniv, and E. Persky, "Estimation of ship's magnetic signature using multidipole modeling method," *IEEE Trans. Magn.*, vol. 57, no. 5, pp. 1–8, May 2021.
- [4] J. Kuang, T. Li, Q. Chen, B. Zhou, and X. Niu, "Consumer-grade inertial measurement units enhanced indoor magnetic field matching positioning scheme," *IEEE Trans. Instrum. Meas.*, vol. 72, pp. 1–14, Nov. 2022.
- [5] G. Liu, B. Yu, L. Huang, L. Shi, X. Gao, and L. He, "Human-interactive mapping method for indoor magnetic based on low-cost MARG sensors," *IEEE Trans. Instrum. Meas.*, vol. 70, pp. 1–10, Jan. 2021.
- [6] A. Ahmed, S. A. Abbasi, N. L. Gharamaleki, J.-Y. Kim, and H. Choi, "MagMaps: An economical, Lego-like approach for real-time magnetic field mapping using commercial magnetic sensors," *IEEE Trans. Instrum. Meas.*, vol. 72, pp. 1–9, Dec. 2022.
- [7] Y. Lu, D. Wei, and X. Ji, "A review of geomagnetic positioning methods," *J. Navig., Posit. Timing*, vol. 9, no. 2, pp. 118–1301, 2022.
- [8] Y. Wang, J. Kuang, T. Liu, X. Niu, and J. Liu, "CrowdMagMap: Crowdsourcing-based magnetic map construction for shopping mall," *IEEE Internet Things J.*, vol. 11, no. 3, pp. 5362–5373, Feb. 2024.
- [9] G.-X. Liu, L.-F. Shi, S. Chen, and Z.-G. Wu, "Focusing matching localization method based on indoor magnetic map," *IEEE Sensors J.*, vol. 20, no. 17, pp. 10012–10020, Sep. 2020.
- [10] J. Kuang, T. Li, and X. Niu, "Magnetometer bias insensitive magnetic field matching based on pedestrian dead reckoning for smartphone indoor positioning," *IEEE Sensors J.*, vol. 22, no. 6, pp. 4790–4799, Mar. 2022.
- [11] L. Hao, K. Yu, and Y. Lin, "Method and performance analysis of geomagnetic indoor positioning based on proximity point features," *J. Navig., Posit. Timing*, vol. 9, no. 3, pp. 100–1066, 2022.
- [12] G. Wang, X. Wang, J. Nie, and L. Lin, "Magnetic-based indoor localization using smartphone via a fusion algorithm," *IEEE Sensors J.*, vol. 19, no. 15, pp. 6477–6485, Aug. 2019.
- [13] L.-F. Shi, R. He, and B.-L. Feng, "Indoor localization scheme using magnetic map for smartphones," *Wireless Pers. Commun.*, vol. 122, pp. 1329–1347, Jan. 2022.
- [14] Y. Wang, J. Kuang, Y. Li, and X. Niu, "Magnetic field-enhanced learning-based inertial odometry for indoor pedestrian," *IEEE Trans. Instrum. Meas.*, vol. 71, pp. 1–13, Jun. 2022.
- [15] L.-F. Shi, M.-X. Yu, and W. Yin, "PDR/geomagnetic fusion localization method based on AOFA-improved particle filter," *IEEE Trans. Instrum. Meas.*, vol. 71, pp. 1–9, Nov. 2021.
- [16] L.-F. Shi, B.-L. Feng, Y.-F. Dai, G.-X. Liu, and Y. Shi, "Pedestrian indoor localization method based on integrated particle filter," *IEEE Trans. Instrum. Meas.*, vol. 72, pp. 1–10, Jan. 2023.
- [17] X. Shi, Z. Jia, H. Geng, S. Liu, and Y. Li, "Deep learning inversion for multivariate magnetic data," *IEEE Trans. Geosci. Remote Sens.*, vol. 62, Nov. 2023, Art. no. 5900110.
- [18] N. Lee and D. Han, "Magnetic indoor positioning system using deep neural network," in *Proc. Int. Conf. Indoor Posit. Indoor Navig. (IPIN)*, Sapporo, Japan, 2017, pp. 1–8.
- [19] A. B. Adege, H. P. Lin, G. B. Tarekgn, Y. Y. Munaye, and L. Yen, "An indoor and outdoor positioning using a hybrid of support vector machine and deep neural network algorithms," *J. Sensors*, vol. 2018, no. 1, pp. 1–12, 2018.
- [20] A. Khan, V. Ghorbanian, and D. Lowther, "Deep learning for magnetic field estimation," *IEEE Trans. Magn.*, vol. 55, no. 6, pp. 1–4, Jun. 2019.
- [21] S. Yan et al., "Deep learning-based geomagnetic navigation method integrated with dead reckoning," *Remote Sens.*, vol. 15, no. 17, p. 4165, 2023.
- [22] Y. Pang, Z. Zhou, X. Pan, and N. Song, "An INS/geomagnetic integrated navigation method for coarse estimation of positioning error and search area adaption applied to high-speed aircraft," *IEEE Sensors J.*, vol. 23, no. 7, pp. 7766–7775, Apr. 2023.
- [23] W. Song et al., "Magnetic sensor array based on coordinate measuring and differential evolution algorithm," *IEEE Sensors J.*, vol. 23, no. 17, pp. 19137–19144, Sep. 2023.
- [24] N. Fischer, J. Kriegbaum, D. Berwanger, and F. Mathis-Ullrich, "Compliant Hall-effect sensor array for passive magnetic instrument tracking," *IEEE Sensors Lett.*, vol. 7, no. 3, pp. 1–4, Mar. 2023.
- [25] C. Huang, G. Hendeby, H. Fourati, C. Prieur, and I. Skog, "MAINS: A magnetic-field-aided inertial navigation system for indoor positioning," *IEEE Sensors J.*, vol. 24, no. 9, pp. 15156–15166, May 2024.
- [26] Y. Cui, Z. Xiong, X. Li, L. Xing, Y. Sun, and Y. Qian, "A pedestrian SLAM scheme grounded in inertial-based map and magnetic field map," *IEEE Sensors J.*, vol. 24, no. 5, pp. 6500–6514, Mar. 2024.
- [27] F. Liu and B. Yan, "Local magnetic field inversion based on the modified L-curve model function method," *IEEE Sensors J.*, vol. 24, no. 18, pp. 29232–29242, Sep. 2024.
- [28] A. Solin, K. Kok, N. Wahlström, T. B. Schön, and S. Särkkä, "Modeling and interpolation of the ambient magnetic field by Gaussian processes," *IEEE Trans. Robot.*, vol. 34, no. 4, pp. 1112–1127, Aug. 2018.
- [29] I. Wardinski et al., "Geomagnetic core field models and secular variation forecasts for the 13th International Geomagnetic Reference Field (IGRF-13)," *Earth, Planets Space*, vol. 72, pp. 1–12, Oct. 2020.